

# Centimeter-Long Weavable Fibers of Carbon Nanotubes with Giant Thermoelectric Power Factor

**Natsumi Komatsu**

Rice University

**Yota Ichinose**

Tokyo Metropolitan University

**Oliver Dewey**

Rice University

**Lauren Taylor**

Rice University

**Mitchell Trafford**

Rice University

**Yohei Yomogida**

Tokyo Metropolitan University

**Geoff Wehmeyer**

Rice University

**Matteo Pasquali**

Rice University <https://orcid.org/0000-0001-5951-395X>

**Kazuhiro Yanagi**

Tokyo Metropolitan University <https://orcid.org/0000-0002-7609-1493>

**Junichiro Kono** (✉ [kono@rice.edu](mailto:kono@rice.edu))

Rice University <https://orcid.org/0000-0002-4195-0577>

---

## Article

**Keywords:** Low-dimensional Materials, Charge Carrier Confinement, Macroscopic Assemblies, van Hove Singularity

**Posted Date:** March 22nd, 2021

**DOI:** <https://doi.org/10.21203/rs.3.rs-334346/v1>

**License:** © ⓘ This work is licensed under a Creative Commons Attribution 4.0 International License.

[Read Full License](#)

---

**Version of Record:** A version of this preprint was published at Nature Communications on August 13th, 2021. See the published version at <https://doi.org/10.1038/s41467-021-25208-z>.

# Centimeter-Long Weavable Fibers of Carbon Nanotubes with Giant Thermoelectric Power Factor

Natsumi Komatsu,<sup>1</sup> Yota Ichinose,<sup>2</sup> Oliver S. Dewey,<sup>3</sup> Lauren W. Taylor,<sup>3</sup> Mitchell A. Trafford,<sup>3</sup> Yohei Yomogida,<sup>2</sup> Geoff Wehmeyer,<sup>4,5</sup> Matteo Pasquali,<sup>3,5,6,7</sup> Kazuhiro Yanagi,<sup>2</sup> and Junichiro Kono<sup>1,7,8,\*</sup>

<sup>1</sup>*Department of Electrical and Computer Engineering, Rice University, Houston, Texas, USA*

<sup>2</sup>*Department of Physics, Tokyo Metropolitan University, Tokyo, Japan*

<sup>3</sup>*Department of Chemical and Biomolecular Engineering, Rice University, Houston, Texas, USA*

<sup>4</sup>*Department of Mechanical Engineering, Rice University, Houston, Texas, USA*

<sup>5</sup>*Carbon Hub, Rice University, Houston, Texas, USA*

<sup>6</sup>*Department of Chemistry, Rice University, Houston, Texas, USA*

<sup>7</sup>*Department of Materials Science and NanoEngineering, Rice University, Houston, Texas, USA*

<sup>8</sup>*Department of Physics and Astronomy, Rice University, Houston, Texas, USA*

\*To whom correspondence should be addressed; E-mail: kono@rice.edu.

15 **Low-dimensional materials have recently attracted much interest as thermoelectric materials**  
16 **because of their charge carrier confinement leading to thermoelectric performance enhance-**  
17 **ment. Carbon nanotubes are promising candidates because of their one-dimensionality in**  
18 **addition to their unique advantages such as flexibility and light weight. However, preserving**  
19 **the large power factor of individual carbon nanotubes in macroscopic assemblies has been**  
20 **challenging, primarily due to poor sample morphology and a lack of proper Fermi energy**  
21 **tuning. Here, we report an unprecedentedly high value of power factor ( $14\pm 5 \text{ mWm}^{-1}\text{K}^{-2}$ )**  
22 **for centimeter-long weavable fibers of aligned carbon nanotubes with ultrahigh electrical and**  
23 **thermal conductivity. Our theoretical simulations show that the observed giant power fac-**  
24 **tor originates from the one-dimensional quantum confinement of charge carriers, appearing**  
25 **when the Fermi energy is near a van Hove singularity in the electronic density of states. We**  
26 **fabricated a textile thermoelectric generator based on these carbon nanotube fibers, which**  
27 **demonstrated high thermoelectric performance, weavability, and scalability. The giant power**  
28 **factor we observed make these fibers strong candidates for the emerging field of thermoelec-**  
29 **tric active cooling, which requires a large thermoelectric power factor and a large thermal**  
30 **conductivity at the same time.**

## 31 Introduction

32 Thermoelectric (TE) materials convert heat into electricity and vice versa, offering great potential  
33 for waste heat recovery and solid-state cooling<sup>1</sup>. TE materials are usually evaluated by the  $ZT$  fac-  
34 tor, defined as  $ZT = (S^2\sigma T)/\kappa$ , where  $S$  is the Seebeck coefficient,  $\sigma$  is the electrical conductivity,  
35  $\kappa$  is the thermal conductivity, and  $T$  is the temperature. While previous studies on thermoelectric  
36 materials have primarily focused on reducing  $\kappa$  to improve  $ZT$ , enhancing the power factor ( $PF$ ),  
37 defined as  $PF = S^2\sigma$ , is more important for certain applications. For examples, for the energy  
38 harvesting application, large  $PF$  is crucial for maximizing the output power density when the heat  
39 source is unlimited (such as solar heat and industrial waste heat)<sup>2-4</sup>. Furthermore,  $PF$  must be  
40 large for so-called active cooling<sup>5,6</sup>, in which the Peltier effect is leveraged to enhance the heat  
41 flow rates from the hot side to the cold side. This active cooling mode is promising for electronics  
42 thermal management applications, and is distinct from the more traditional refrigeration opera-  
43 tional mode in which heat is pumped from the cold side to the hot side via the Peltier effect<sup>5,6</sup>.  
44 The maximum hot-side heat flow rate in active cooling is proportional to the effective thermal con-  
45 ductivity  $\kappa_{\text{eff}}$ , defined as<sup>5</sup>  $\kappa_{\text{eff}} = \kappa + \frac{PF \cdot T_{\text{H}}^2}{2\Delta T}$ , where  $T_{\text{H}}$  is the hot-side temperature and  $\Delta T$  is the  
46 temperature difference between the two sides, suggesting that the active cooling requires large  $\kappa$   
47 together with large  $PF$ , instead of high  $ZT$ .

48 In addition to the basic TE properties, practical applications require other considerations,  
49 such as toxicity, flexibility, and scalability<sup>7,8</sup>. Conventional inorganic TE materials such as  $\text{Bi}_2\text{Te}_3$   
50 and their alloys have shown high performance, e.g.,  $ZT \sim 1.2$  and  $PF \sim 4.5 \text{ mWm}^{-1}\text{K}^{-2}$  at

51 room temperature <sup>9</sup>. However, their toxicity, scarcity, and rigidity prevent their wide use. On the  
52 other hand, organic materials are safe, flexible, and inexpensive, but they have exhibited small  $PF$   
53 values <sup>7</sup>. These issues have resulted in a search for organic-like materials with inorganic-like TE  
54 performance.

55 Low-dimensional materials are believed to hold the key to achieving this goal. Recent stud-  
56 ies have reported record-high  $PF$  values at room temperature for two-dimensional (2D) materi-  
57 als: monolayer graphene [36.6  $\text{mWm}^{-1}\text{K}^{-2}$  at 290 K <sup>10</sup>] and ultrathin FeSe [26  $\text{mWm}^{-1}\text{K}^{-2}$  at  
58 280 K <sup>11</sup>]. However, such demonstrations have been limited to small flakes, and whether they are  
59 scalable for practical applications is questionable. One-dimensional (1D) materials such as carbon  
60 nanotubes (CNTs) are expected to possess even better TE properties <sup>12</sup>. 1D quantum confinement of  
61 charge carriers leads to enhanced TE performance through a narrow carrier distribution achieved  
62 when the Fermi energy,  $E_F$ , is near a 1D van Hove singularity (VHS) in the density of states  
63 (DOS) <sup>13</sup>. Furthermore, in recent years, significant improvements have been made in fabricating  
64 macroscopically ordered CNT assemblies <sup>14</sup> with superb thermal <sup>15,16</sup> and mechanical properties <sup>17</sup>,  
65 suggesting that CNTs can be used for creating an ideal TE materials with high TE performance,  
66 flexibility and scalability simultaneously.

67 Single-wall CNTs (SWCNTs) can be either semiconducting or metallic, depending on their  
68 chirality,  $(n,m)$  <sup>18</sup>. For TE device applications, mainly semiconducting SWCNTs have been studied  
69 because of their larger  $S$  compared to metallic SWCNTs <sup>19,20</sup>. As in any semiconductor, however,  
70 the maximum  $S$  is achieved when  $E_F$  is near the charge neutrality point (CNP) in the middle of

71 the bandgap, where  $\sigma$  (and thus  $PF$ ) is negligibly small because the DOS is zero. An attempt  
72 to increase  $\sigma$  by moving  $E_F$  toward a band-edge decreases  $S$ ; this trade-off between  $S$  and  $\sigma$  is a  
73 well-known dilemma for TE material development<sup>21</sup>. Recently, Ichinose *et al.* have experimentally  
74 demonstrated that metallic SWCNTs can show higher  $PF$  than semiconducting SWCNTs when  
75  $E_F$  is in the vicinity of a VHS through simultaneous enhancement of  $\sigma$  and  $S$ <sup>22</sup>. The same scenario  
76 holds for a mixture of semiconducting and metallic SWCNTs, and a theoretical study predicts a  
77  $PF$  higher than  $100 \text{ mWm}^{-1}\text{K}^{-2}$ <sup>23</sup>. However, experimentally measured  $PF$  for CNT assemblies  
78 has remained small<sup>8</sup>, presumably due to low  $\sigma$  originating from poor sample morphology.

79 Here, we studied the TE properties of centimeter-long weavable CNT fibers. These neat CNT  
80 fibers simultaneously possess a high degree of CNT alignment, a high density, a high CNT aspect  
81 ratio (length/diameter), and a low level of impurities<sup>16</sup>, leading to ultrahigh electrical conductivity,  
82  $\sigma > 10 \text{ MSm}^{-1}$ <sup>15</sup>. We tuned  $E_F$  to the vicinity of a 1D VHS through chemical treatment to  
83 maximize  $S$ , obtaining  $PF$  as high as  $14 \pm 5 \text{ mWm}^{-1}\text{K}^{-2}$ . This is the highest  $PF$  value achieved  
84 for any CNT system and is comparable to the highest values reported for 2D materials and of bulk  
85 materials<sup>10,11</sup>. We developed a theoretical model to explain this high  $PF$  value and validated it  
86 with finer  $E_F$  tuning using electrolyte gating. Finally, we demonstrated weavability and scalability  
87 by fabricating a textile TE generator based on these CNT fibers, which produced enough power to  
88 turn on a light-emitting diode (LED).

## 89 Results and Discussions

90 **Giant power factor in ultrahigh-conductivity CNT fibers.** Densely packed and highly aligned  
91 fibers of CNTs were produced by a solution spinning method<sup>15,16</sup>. The fiber average diameter was  
92  $8.9\pm 0.9\ \mu\text{m}$  (see Figure 1a), containing double-wall CNTs (DWCNTs) with an average outer-wall  
93 diameter of  $1.8\pm 0.2\ \text{nm}$  and an average inner-wall diameter of  $0.9\pm 0.1\ \text{nm}$ . Additional information  
94 on the CNT fiber can be found in Ref.<sup>15</sup>. We chemically treated as-produced CNT fibers to tune  $E_F$   
95 (conditions summarized in Supplementary Table S1). The as-produced CNT fibers were heavily  $p$ -  
96 doped with residual acid during the solution spinning process<sup>16</sup>, and exhibited  $\sigma$  of  $11\pm 2\ \text{MSm}^{-1}$ .  
97 Doping an as-produced CNT fiber with iodine monochloride (ICl) increased the value of  $\sigma$  to  
98  $16\pm 3\ \text{MSm}^{-1}$  through further  $p$ -type doping, while annealing them at a temperature of  $350\ ^\circ\text{C}$   
99 ( $500\ ^\circ\text{C}$ ) decreased  $\sigma$  to  $5.6\pm 1.1\ \text{MSm}^{-1}$  ( $2.7\pm 0.5\ \text{MSm}^{-1}$ ) through dedoping.

100 We measured the  $\sigma$  and  $S$  of these CNT fibers at room temperature under vacuum using  
101 an experimental setup schematically shown in Figure 1b; see Supplementary information (SI) for  
102 more details about the measurements. The measured  $S$  values were all positive, indicating that  
103 the carrier type was  $p$ -type in these samples. Figure 1c shows a monotonic decrease of  $S$  with  
104 increasing  $\sigma$ , resulting in a decrease of  $PF$  with  $\sigma$  (Figure 1d). The highest  $S$  was obtained for the  
105 CNT fiber annealed at  $500\ ^\circ\text{C}$ , and the measurements were repeated for three samples to ensure  
106 reproducibility. The average  $S$  of the three samples (all annealed at  $500\ ^\circ\text{C}$ ) was  $68.0\pm 0.3\ \mu\text{VK}^{-1}$ ,  
107 corresponding to an average (maximum)  $PF$  of  $12\pm 2\ \text{mWm}^{-1}\text{K}^{-2}$  ( $14\pm 5\ \text{mWm}^{-1}\text{K}^{-2}$ ).

108 This maximum  $PF$  value,  $14\pm 5\ \text{mWm}^{-1}\text{K}^{-2}$ , is the highest value ever achieved for any

109 CNT sample. Figure 1e summarizes the room-temperature  $PF$  values reported for different CNT  
110 systems with  $\sigma$ . The highest  $PF$  among CNT systems has been  $\sim 3 \text{ mWm}^{-1}\text{K}^{-2}$ , achieved for  
111 an unsorted benzyl viologen doped CNT web <sup>24</sup> and CNT-filled polymer nanocomposites <sup>25</sup>. Fur-  
112 thermore, our value is over three times larger than that of  $\text{Bi}_2\text{Te}_3$ , the commercially used inor-  
113 ganic  $p$ -type TE material ( $\sim 4.5 \text{ mWm}^{-1}\text{K}^{-2}$ ) <sup>9</sup>, and is comparable to the highest  $PF$  achieved at  
114 room temperature by 2D materials: monolayer graphene ( $36.6 \text{ mWm}^{-1}\text{K}^{-2}$ ) <sup>10</sup> and ultrathin FeSe  
115 ( $26.0 \text{ mWm}^{-1}\text{K}^{-2}$ ) <sup>11</sup>.

116 Furthermore, the high PF observed is promising for use in active cooling, leveraging the  
117 high thermal conductivity ( $580 \text{ Wm}^{-1}\text{K}^{-1}$ ) of the CNT fibers <sup>16</sup>. TE active cooling requires a  
118 material with large  $\kappa$  and large  $PF$ , simultaneously, to maximize  $\kappa_{\text{eff}}$ . However, no existing TE  
119 materials satisfy this requirement, as shown in Figure 1f. Conventional TE cooling materials have  
120 relatively large  $PF$ , but small  $\kappa$ . Adams *et al.* used a magnon-drag metal (Co) and a Kondo-effect  
121 metal ( $\text{CePd}_3$ ), which showed  $\kappa_{\text{eff}}$  of  $780 \text{ Wm}^{-1}\text{K}^{-1}$  and  $360 \text{ Wm}^{-1}\text{K}^{-1}$  at 300 K with a  $\Delta T$  of  
122 1 K, respectively <sup>5</sup>. Given same temperature difference ( $\Delta T = 1 \text{ K}$ ), the  $\kappa_{\text{eff}}$  of our CNT fibers  
123 is expected to be  $1,190 \text{ Wm}^{-1}\text{K}^{-1}$ , exceeding those of Co and  $\text{CePd}_3$  as well as conventional TE  
124 materials <sup>26</sup> (see Table S4).

125 **Theoretical model to explain  $E_{\text{F}}$  dependence of TE properties.** To provide insight into the  
126 mechanism that led to the high  $PF$  in our CNT fibers, we developed a theoretical model and per-  
127 formed simulations. We chose four representative SWCNTs with appropriate diameters to describe  
128 the DWCNT fibers: an inner-wall semiconducting SWCNT (S1), an inner-wall metallic SWCNT

129 (M1), an outer-wall semiconducting SWNCT (S2), and an outer-wall metallic SWCNT (M2); see  
 130 Supplementary Table S2. We first calculated the DOS (Figure 2d),  $S$ , electrical conductance  $G$ ,  
 131 and  $PF' \equiv GS^2$  for each individual SWCNT. Next, we modeled a DWCNT as consisting of two  
 132 individual SWCNTs corresponding to the inner and outer nanotubes, while adopting circuit mod-  
 133 els<sup>23,27,28</sup> to approximate our DWCNT fiber. We obtained the combined conductance  $G_p$  ( $G_s$ ) and  
 134 Seebeck coefficient  $S_p$  ( $S_s$ ) for the parallel (series) case. Then we further combined  $S_p$  and  $S_s$   
 135 through  $S_{\text{tot}} = (1 - \beta)S_s + \beta S_p$ <sup>19</sup>, where  $\beta$  is the fraction of the parallel component. We set  $\beta$  to  
 136 be 0.9 and assumed  $G_{\text{tot}} = G_p$  to best fit the experimental data. More details about the calculation  
 137 methods are given in SI.

138 Calculated  $G$ ,  $S$ , and  $PF'$  using our model as a function of  $E_F$  are shown in Figures 2a, b,  
 139 and c, respectively. Their behaviors qualitatively differ from those of individual semiconducting  
 140 SWCNTs such as S1 and S2 (Supplementary Figure S9). As shown in Figure 2a,  $G$  is finite even  
 141 when the  $E_F$  is inside the bandgap. Moreover, maximum  $|S|$  appears when  $E_F$  is in the vicinity  
 142 of the first VHS of S2, not when  $E_F$  is near the CNP (Figure 2b). This is because the peak of  
 143  $|S|$  near the CNP, expected for S1 or S2 alone, is suppressed in our combined system due to  
 144 their nearly zero conductance inside the bandgap (Supplementary Equation S9). Figures 2b and c  
 145 demonstrate that  $S$  and  $PF'$  show a maximum value when the  $E_F$  is around the first VHS of S2,  
 146 and the next peak appears when the  $E_F$  is around the second VHS of S2 (overlapping with the first  
 147 VHS of S1), consistent with previous studies<sup>22,23</sup>. In addition, we conducted systematic optical  
 148 spectroscopy measurements to estimate the  $E_F$  of four chemically treated samples for comparison  
 149 with the calculations; see SI for details. Figures 2a, b, and c show experimental  $\sigma$ ,  $S$  and  $PF$ ,

150 respectively, as a function of estimated  $E_F$ . Experimental data and calculated values demonstrated  
151 excellent qualitative agreement, proving that the highest value of  $PF$  observed for the CNT fibers  
152 is a result of  $E_F$  being tuned to the vicinity of the VHS.

153 To validate these calculations, we further measured the  $\sigma$ ,  $S$ , and  $PF$  of a CNT fiber while  
154 varying  $E_F$  using the electrolyte gating technique<sup>22,29</sup>. Specifically, we injected electrons or holes  
155 into the CNT fiber to shift the  $E_F$  by changing the gate voltage  $V_G$ . The CNT fiber was annealed  
156 before the measurements to remove residual dopants. Figures 2e and f show the measured  $\sigma$  and  
157  $S$  as a function of  $V_G$ , respectively. In both plots, the CNP corresponds to  $V_G = 0$ ; i.e., the  
158 experimental  $V_G$  values were shifted such that  $\sigma$  becomes minimum at  $V_G = 0$ . The observation  
159 of both positive and negative  $S$  and a transistor-like behavior of  $\sigma$  indicate that  $E_F$  was tuned from  
160 the  $p$ -type regime to the  $n$ -type regime. The  $S$  values presented in Figure 2f are lower than those  
161 in Figure 1c because the sample was immersed in the ionic liquid. Figure 2g plots the calculated  
162  $S$  (experimental  $S$ ) as a function of calculated  $G$  (experimental  $\sigma$ ) for direct comparison of our  
163 calculations with the gate-dependent data. The overall behavior ( $S$  increases, decreases, and then  
164 increases again with  $\sigma$ ) is well reproduced, validating our model.

165 These results highlight the promising property of our CNT fibers for TE applications, i.e.,  
166 their ability to possess large  $S$  and  $\sigma$  simultaneously. Unlike conventional semiconductors, CNTs  
167 can acquire a large value of  $S$  through enhancement by the 1D VHS, irrespective of whether  $\sigma$  is  
168 large. In fact, our calculated maximum  $PF'$  corresponds to a  $PF$  of  $2.0 \text{ Wm}^{-1}\text{K}^{-2}$  with the same  
169  $S$  value as in Figure 2b ( $73 \mu\text{VK}^{-1}$ ) and estimated  $\sigma$  ( $3.7 \times 10^8 \text{ Sm}^{-1}$ ) assuming a diameter of

170 1.73 nm and an aspect ratio of 6,700. This suggests that, by further enhancing the  $\sigma$ , the same CNT  
171 fibers can theoretically provide a  $PF$  value larger than  $1 \text{ Wm}^{-1}\text{K}^{-2}$ . Note that  $\sigma$  of  $10^8 \text{ Sm}^{-1}$  is  
172 well expected within ten years by the current  $\sigma$  improvement rate of 26 %/year<sup>15</sup>.

173 **Textile TE generator based on centimeter-long weavable CNT threads.** The high  $PF$  value  
174 that we found, in addition to their weavability and scalability, make CNT fibers promising building  
175 blocks for the emerging technology of fiber and textile electronics<sup>30–33</sup>. CNT fibers are not only  
176 weavable by using a commercial sewing machine but also washable<sup>34</sup>. These unique properties are  
177 difficult to achieve using other functional fibers. Here, we fabricated a high-performance textile TE  
178 generator based on CNT threads sewn into a fabric. The CNT thread had the total length of a few  
179 meters, was composed of 21 filaments, and each filament had an average diameter of  $22 \pm 1.0 \mu\text{m}$ ;  
180 see Methods for more details about the CNT threads. We sewed the CNT threads and stainless  
181 steel threads into a fabric (100% cotton) using a sewing machine such that the CNT threads were  
182 connected electrically in series and thermally in parallel, as shown in Figures 3a and b. It showed  
183 great flexibility, as shown in the inset of Figure 3d. We generated a temperature difference,  $\Delta T$ ,  
184 across the device by heating one side ( $T_{\text{hot}}$ ) with hotplates while keeping the other side ( $T_{\text{cold}}$ ) at  
185 room temperature. The CNT threads generated power through the Seebeck effect, while the steel  
186 threads provided electrical connections.

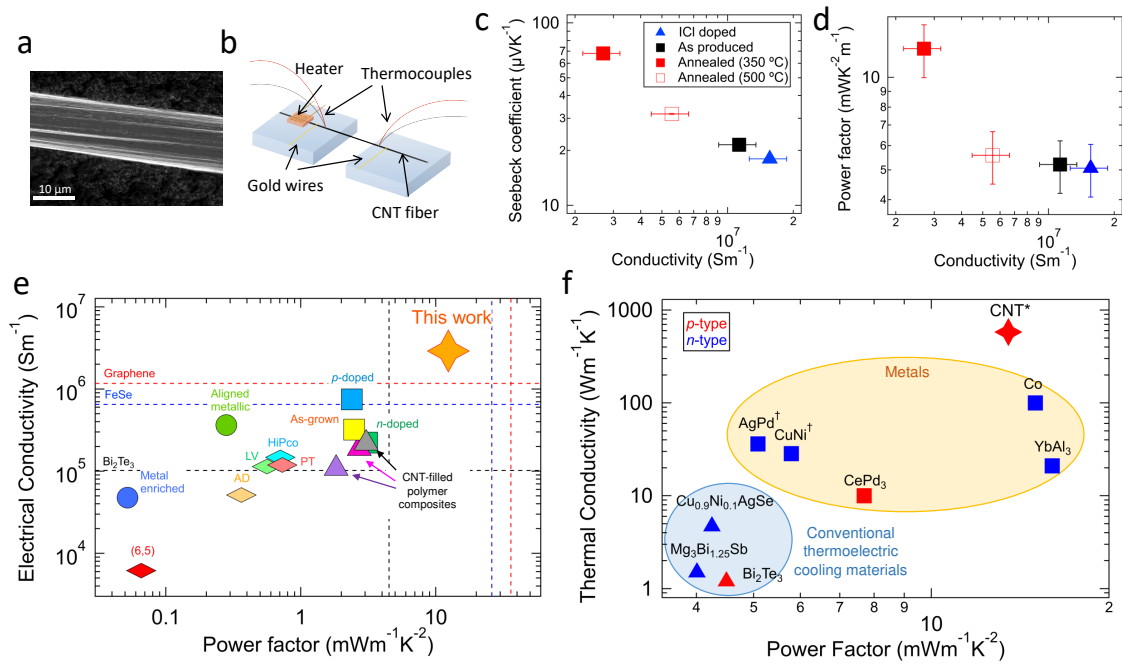
187 Using this CNT-based textile TE generator, we demonstrated powering of a LED (see also  
188 Supplementary Video S1). The entire device consisted of sixty CNT threads connected, and we  
189 utilized capacitors to drive the LED with a bootstrap converter, as shown in Supplementary Fig-

190 ure S5; see SI for details. With a  $\Delta T$  of  $>50$  K, the textile TE generator provided a high enough  
191 voltage to light up the LED, as shown in Figure 3c. Figure 3d demonstrates the output voltage and  
192 power of the device with sixty CNT threads. The device generated a voltage of 83 mV and a power  
193 of  $5.0 \mu\text{W}$  when a  $\Delta T$  of 60 K was applied. Further improvements on the device architecture can  
194 be made to achieve out-of-plane energy harvesting and cooling, which are promising for wearable  
195 devices<sup>35,36</sup>.

## 196 **Conclusion**

197 In summary, we studied the thermoelectric properties of aligned CNT fibers with an ultrahigh  
198 electrical conductivity ( $> 10^6 \text{ Sm}^{-1}$ ) by varying the Fermi energy and obtained a maximum power  
199 factor of  $14 \pm 5 \text{ mWm}^{-1}\text{K}^{-2}$ . Our theoretical study demonstrated that the ultrahigh power factor  
200 appeared when the Fermi energy was near a van Hove singularity in 1D electronic density of  
201 states, and suggested that it can be further improved by electrical conductivity enhancement. We  
202 demonstrated the weavability and scalability of the CNT fibers as a novel TE material by fabricating  
203 a textile thermoelectric generator sewn into a fabric. The coexistence of giant thermoelectric power  
204 factor, flexibility, and scalability in the CNT fibers promises an unprecedentedly diverse range of  
205 TE applications, including the thermoelectric active cooling application, where both a large power  
206 factor and a large thermal conductivity are required.

207 **Figures**



208

209

210 **Fig. 1. Thermoelectric properties of densely packed and highly aligned CNT fibers.**

211

212

213

214

215

216

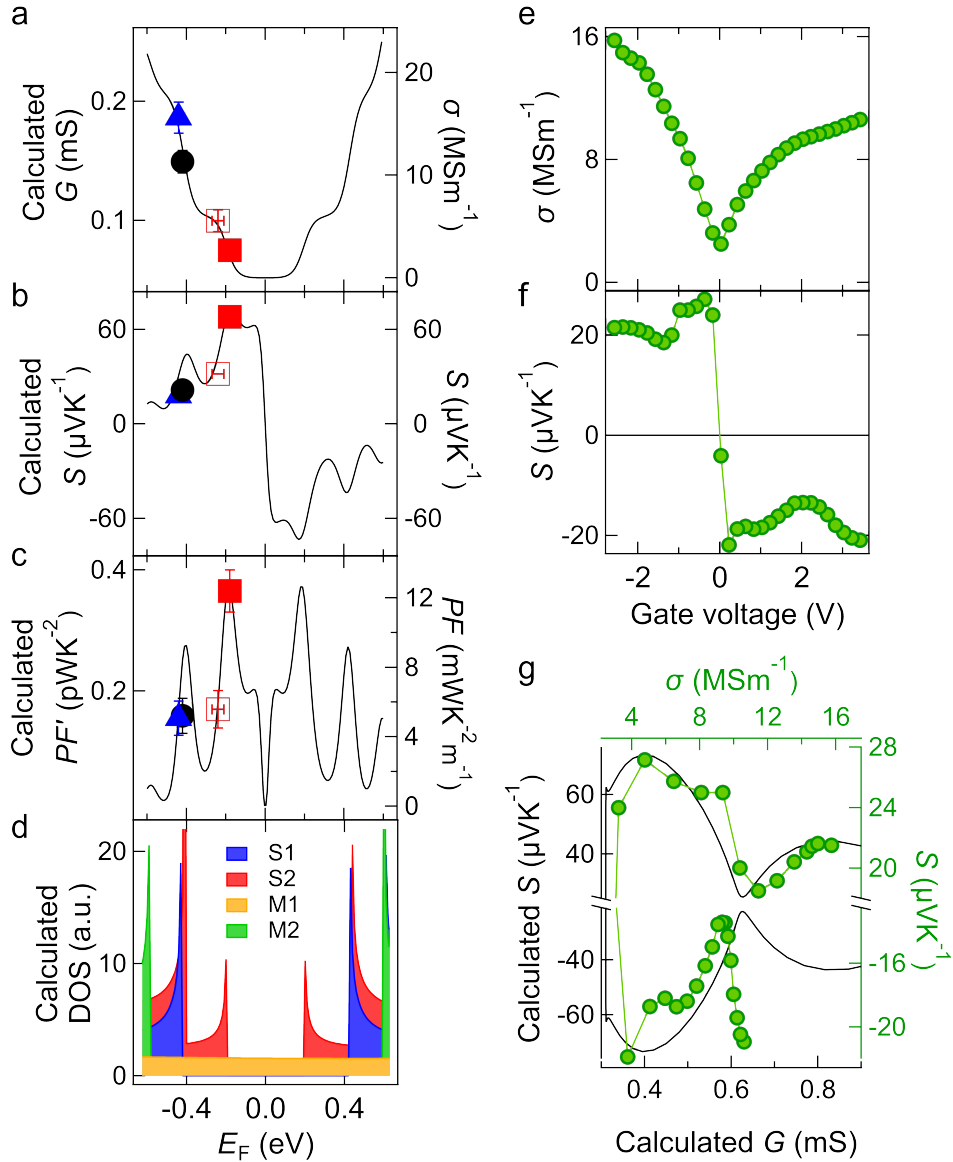
217

218

219

image of a CNT fiber. **b**, Schematic of the experimental setup used for measuring the electrical conductivity ( $\sigma$ ) and Seebeck coefficient ( $S$ ) of CNT fibers. **c**, Measured  $S$  and **d**, corresponding power factor ( $PF = S^2\sigma$ ) as a function of  $\sigma$  for four CNT fibers that underwent different chemical treatments: ICl doped (solid blue triangles), as-produced (solid black circles), annealed at 350 °C (open red squares), and annealed at 500 °C (solid red squares). The values are summarized in Supplementary Table S1. **e**, Comparison of reported  $PF$  values for various CNT samples with  $\sigma$ . The plot includes unsorted CNTs (as-grown (yellow square)<sup>37</sup>,  $p$ -doped (blue square)<sup>38</sup> and  $n$ -doped (green square)<sup>24</sup>), semiconductor-enriched SWNCTs (originally produced by arc-discharge (AD) (orange diamond)<sup>39</sup>, by laser vaporiza-

220 tion (LV) (green diamond) <sup>39</sup>, by HiPco (blue diamond) <sup>39</sup>, by plasma torch (PT) (pink dia-  
221 mond) <sup>39</sup>, and (6,5) SWCNTs (red diamond) <sup>22</sup>), metal-enriched SWCNTs (un-aligned films  
222 (blue circle)<sup>22</sup> and aligned films (green circle) <sup>22</sup>), and CNT-filled polymer nanocomposites  
223 (PANI/graphene/PANI/DWCNT (purple triangle) <sup>40</sup>, PANI/graphene-PEDOT:PSS/PANI/DWCNT-  
224 PEDOT:PSS (pink triangle) <sup>41</sup>, and PANI/graphene/PANI/DWCNT (gray triangle) <sup>25</sup>). Values  
225 are summarized in Supplementary Table S3. *PF* values of Bi<sub>2</sub>Te<sub>3</sub> alloys <sup>9</sup>, graphene <sup>10</sup>, and  
226 FeSe <sup>11</sup> serve as references. **f**, Comparison of reported *PF* values for representative materi-  
227 als with  $\kappa$  at 300 K with a  $\Delta T$  of 1 K. The plot includes metals (squares) (Co <sup>42</sup>), YbAl<sub>3</sub> <sup>43</sup>,  
228 CePd<sub>3</sub> <sup>44</sup>, CuNi <sup>45</sup>, and AgPd <sup>45</sup>) and conventional thermoelectric cooling materials (triangles)  
229 (Bi<sub>2</sub>Te<sub>3</sub> <sup>9</sup>, Cu<sub>0.9</sub>Ni<sub>0.1</sub>AgSe <sup>46</sup>, and Mg<sub>3</sub>Bi<sub>1.25</sub>Sb <sup>47</sup>). *p*-type (*n*-type) materials are highlighted  
230 in red (blue). † The temperature was at 400 K because values at 300 K were not available.  
231 \* Thermal conductivity value was taken from Ref. <sup>16</sup>. Values are summarized in Supplemen-  
232 tary Table S4.



233

234

**Fig. 2. Explaining the  $E_F$  dependent TE properties of CNT fibers through modeling.**

235

**a**, Calculated conductance  $G$ , **b**,  $S$ , and **c**,  $PF' \equiv GS^2$  (left) versus  $E_F$ . Experimental data

236

from four chemically treated samples are shown by different symbols on the right axis: ICI

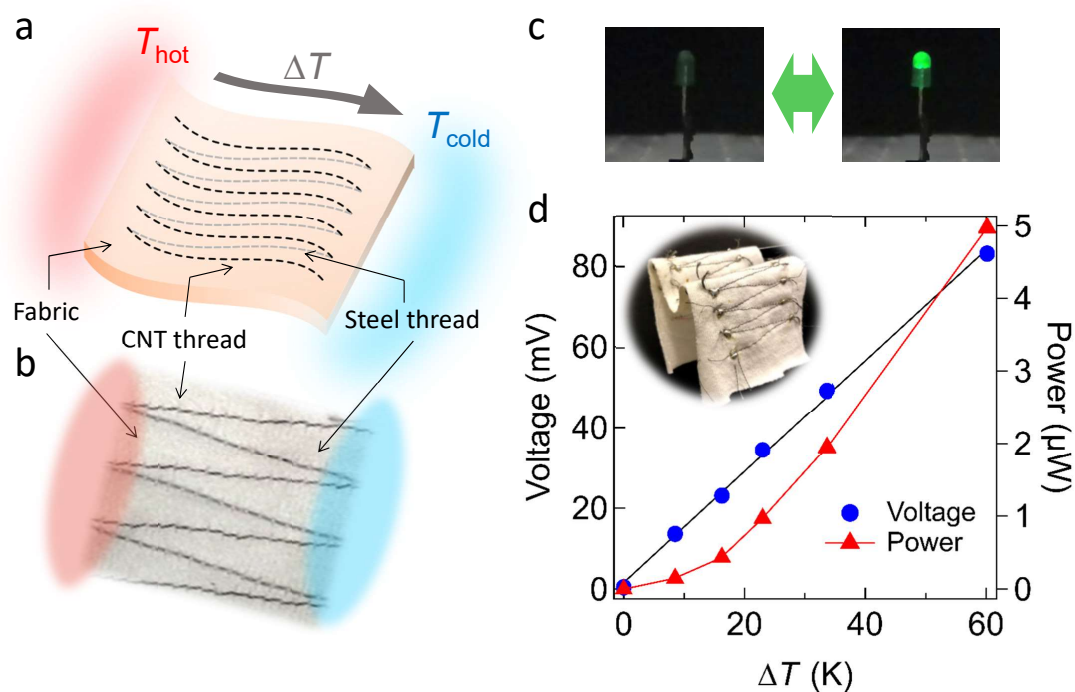
237

doped (solid blue triangle), as-produced (solid black circle), annealed at 350 °C (open red

238

square), and annealed at 500 °C (solid red square). **d**, the DOS of four representative SWCNTs

239 contained in our CNT fibers, S1 (blue), S2 (red), M1 (orange), and M2 (green). **e** and **f**, TE  
240 properties tuned by the electrolyte gating technique. **e**, Measured  $\sigma$  and **f**,  $S$  as a function of  
241 gate voltage. **g**, Comparison of calculated  $S$  (left) as a function of  $G$  (bottom) with experimen-  
242 tal  $S$  (right) as a function of  $\sigma$  (top) with an offset in the  $x$ -axis such that the examined range  
243 by the experiments agrees. The calculated  $S$  is plotted with a black line, and the experimental  
244 data for gated samples are shown by a green line with solid circles.



245

246

247

248

249

250

251

252

253

254

**Fig. 3. Textile TE generator based on CNT threads sewn into a fabric.** **a**, Schematic and **b**, photograph of the device. CNT threads (*p*-type thermoelectric generator) and steel threads (for electrical connection) were sewn into a fabric using a sewing machine. The CNT threads were connected electrically in series and thermally in parallel. A temperature difference  $\Delta T$  was applied by heating one side ( $T_{hot}$ ) while keeping the other side ( $T_{cold}$ ) at room temperature. **c**, The entire device was connected to an LED through an amplification circuit and a capacitor. The LED turned on with a  $\Delta T$  of  $\sim 50$  K. **d**, Output voltage and power as a function of applied  $\Delta T$ . The inset shows a folded device, demonstrating its flexibility.

## 255 **Methods**

### 256 **Solution Spinning Method**

257 CNTs were produced by Meijo Nano Carbon Co. and high resolution transmission electron  
258 microscopy (HR-TEM) was performed on the raw CNT material (Supplementary Figure S1a).

259 The average outer wall diameter was  $1.8 \pm 0.2$  nm, the average inner wall diameter was  $0.9 \pm$   
260  $0.1$  nm, and the average number of walls was 1.9. The viscosity-averaged aspect ratio of the  
261 CNTs was  $6700 \pm 100$ , as measured with a capillary thinning extensional rheometer<sup>48</sup>.

262 CNT fibers were spun from chlorosulfonic acid (CSA) (Sigma-Aldrich, 99%), coagulated into  
263 acetone and collected onto a rotating drum, as previously described<sup>15,16</sup>. Unlike other disper-  
264 sion techniques such as ultrasonication and chemical functionalization, this method for disper-  
265 sion does not induce defects in the  $sp^2$  bonding of the CNTs and does not shorten the CNTs.  
266 Supplementary Figure S1b shows a representative scanning electron microscopy (SEM) image  
267 of the surface of the produced CNT fiber, used to measure the average diameter. The average  
268 diameter was  $8.9 \pm 0.9$   $\mu\text{m}$ , and the total length was a few meters.

### 269 **Chemical Treatment to Solution Spun Fibers**

270 Doping: Iodine monochloride (ICl) was introduced to the fiber structure via vapor-phase doping  
271 (evaporate dopant in presence of CNT fiber. The fiber was gently wound around a glass vial  
272 and secured at each end with Kapton tape to prevent tangling. The dopant was handled in a  
273 dry-air glove box to minimize interactions with moisture in the air. The dopant and fibers were  
274 combined at room temperature in a round-bottom flask (RBF) purged with nitrogen gas. The  
275 RBF was sealed and placed under vacuum until the dopant began to evaporate and was placed

276 in a box oven at the doping temperature. The box oven was masked with aluminum foil to  
277 minimize light exposure. After doping, the RBF was removed from the oven and chilled in a  
278 water bath followed by an ice water bath to encourage dopant condensation and crystallization  
279 at the inner wall of the RBF instead of on the CNT fiber. The fiber was immediately removed  
280 from the glass vial and subsequently taped in a folder for storage.

281 **Annealing:** The CNT fibers were annealed in the furnace (ARF-30K, ASH (Asahi Rikagaku))  
282 under vacuum ( $\sim$ mTorr) with a temperature controller (AGC-S, ASH (Asahi Rikagaku)) at the  
283 target temperature (350 °C or 500 °C) for four hours.

#### 284 **Textile Thermoelectric Generator (TEG) Fabrication**

285 The raw CNT material used for the device was produced by Meijo Nano Carbon Co., and the  
286 average diameter was determined to be 1.8 nm with an average of 1.5 walls. The aspect ratio  
287 was 4100. CNT fibers were produced using the same method but using a 2 wt% solution of  
288 CNTs in CSA. The average diameter was  $22.0 \pm 1.0 \mu\text{m}$ . Twenty-one filaments of CNT fibers  
289 were plied together to create a sewing thread.

290 The CNT thread and stainless steel thread (NGW-1pc Conductive Stainless Steel Sewing Thread),  
291 were sewn onto a fabric in 4 cm lengths using a commercial sewing machine (Singer 2277  
292 Tradition). Silver paste (PELCO® Conductive Silver Paint, Ted Pella, Inc.) were applied at  
293 junctions for better electrical connections. Fifteen CNT threads were connected thermally in  
294 parallel and electrically in series to create one TEG unit, and the four units were connected in  
295 series as shown in Figure S4. The resistance of the entire TEG was  $\sim 300 \Omega$ . The cold side was  
296 at room temperature, and the hot side was placed on the hotplates.

### 297 **Thermoelectric Measurement (Without electrolyte gating)**

298 The CNT fiber was suspended between two glass slides. A heater (KFR-02N-120-C1-11N10C2,  
299 Kyowa Dengyo Co.) was attached on one side of the fiber, and thermocouples (KFT(TW)-50-  
300 100-050, ANBE SMT Co.) were fixed on the fiber at the edge of glass slides by silver paste  
301 (D-500 DOTITE, Fujikura Kasei Co.). Gold wires were attached to the fiber, next to the ther-  
302 mocouples, by silver paste. A device picture is shown in Supplementary Figure S2a. Electrical  
303 conductivity and Seebeck coefficient measurements were conducted in a vacuum ( $\sim 10^{-3}$  Pa)  
304 using a vacuum and low-temperature probe station (Grail 10, Nagase Techno Co.). The con-  
305 ductivity was calculated from the measured resistance of the fiber. The Seebeck coefficient was  
306 measured in the same manner as that described in Ref. <sup>29</sup>.

### 307 **Thermoelectric Measurement (With electrolyte gating)**

308 The CNT fiber was transferred onto a glass slide with pre-deposited gold electrodes (thickness  
309  $\sim 100$  nm). A heater, thermocouples and gold wires were fixed on the fiber as described above.  
310 To ensure that no chemical reaction occurs between silver and ionic liquid, insulating sealant  
311 (TSE397-C, Momentive Performance Materials Japan LLC.) covered the silver paste. The  
312 ionic liquid (TMPA-TFSI, Kanto Chemical Co.) was dropped to cover the CNT fiber and gate  
313 electrodes to create an electrolyte gating system. A device picture is shown in Supplementary  
314 Figure S2b. Electrical conductivity and Seebeck coefficient measurements were conducted in  
315 the same system as above. By changing the gate voltage from +3.6 V to -3.2 V, we injected  
316 electrons or holes into the CNT fiber, shifting the  $E_F$ . For the transport measurements, the  
317 source-drain voltage was kept as small as possible (3 mV), and then the transport properties

318 were evaluated in the linear response region. The Seebeck coefficients were always measured  
319 in the same gate-shift direction, such as from positive to negative, in order to eliminate the  
320 influence of hysteresis during the measurements. An offset applied to the experimental  $V_G$   
321 values such that  $\sigma$  becomes minimum at  $V_G = 0$  was 0.5 V. Note that the offset value depends  
322 on the initial doping level of CNT samples.

### 323 **Powering a Light-Emitting Diode (LED) Demonstration**

324 The entire circuit to power an LED is shown in Supplementary Figure S5. It consists of four  
325 TEG units connected electrically in series, five capacitors connected in parallel (total capac-  
326 itance of 16.5 mF), an LED (TEG-DMO, Custom Thermoelectric, LLC), and a single pole  
327 double throw switch. The LED is attached to a uni-polar boost converter circuit (VB0410-1,  
328 TXL Group, Inc.) to convert low voltage to higher values. When the switch is connected to  
329 A, the capacitor is charged by the TEGs. When it switches to B, the capacitor discharges and  
330 lights up the LED (Supplementary Video S1).

### 331 **Textile TEG Output Voltage and Power Measurement**

332 The cold side of the flexible TEG (four TEG units) was at room temperature, and the hot  
333 side was placed on hotplates, which were monitored by the temperature controller (Model 340  
334 Temperature Controller, Lake Shore Cryotronics, Inc.). The target temperature was set on the  
335 hotplate, and we waited until the temperature stabilized. We first directly connected the TEG to  
336 the voltmeter (Series 2400 Source Measure Unit, Keithley) to measure the open circuit voltage  
337 (Figure 2d). We then connected the TEG to a load resistor, and measured the voltage drop  
338 across the load resistor as well as the current through the resistor. Supplementary Figure S6

339 shows the output voltage and power when the temperature difference was 62.5 K. Figure 2d  
340 plots the maximum power, which was obtained when the load resistor value was the same as  
341 the TEG resistance ( $\sim 300$ ).

## References

1. Bell, L. E. Cooling, heating, generating power, and recovering waste heat with thermoelectric systems. *Science* **321**, 1457–1461 (2008).
2. Liu, W. *et al.* n-type thermoelectric material Mg<sub>2</sub>Sn<sub>0.75</sub>Ge<sub>0.25</sub> for high power generation. *Proc. Natl. Acad. Sci. U.S.A* **112**, 3269–3274 (2015).
3. Liu, W., Kim, H. S., Jie, Q. & Ren, Z. Importance of high power factor in thermoelectric materials for power generation application: A perspective. *Scr. Mater.* **111**, 3–9 (2016).
4. Hung, N. T., Hasdeo, E. H., Nugraha, A. R., Dresselhaus, M. S. & Saito, R. Quantum effects in the thermoelectric power factor of low-dimensional semiconductors. *Phys. Rev. Lett.* **117**, 036602 (2016).
5. Adams, M., Verosky, M., Zebarjadi, M. & Heremans, J. Active peltier coolers based on correlated and magnon-drag metals. *Phys. Rev. Appl.* **11**, 054008 (2019).
6. Zebarjadi, M. Electronic cooling using thermoelectric devices. *Appl. Phys. Lett.* **106**, 203506 (2015).
7. Russ, B., Gludell, A., Urban, J. J., Chabinyk, M. L. & Segalman, R. A. Organic thermoelectric materials for energy harvesting and temperature control. *Nat. Rev. Mater.* **1**, 1–14 (2016).
8. Blackburn, J. L., Ferguson, A. J., Cho, C. & Grunlan, J. C. Carbon-Nanotube-Based Thermoelectric Materials and Devices. *Adv. Mater.* **30**, 1704386 (2018).
9. Poudel, B. *et al.* High-thermoelectric performance of nanostructured bismuth antimony telluride bulk alloys. *Science* **320**, 634–638 (2008).

- 363 10. Duan, J. *et al.* High thermoelectric power factor in graphene/hbn devices. *Proc. Natl. Acad.*  
364 *Sci. U.S.A.* **113**, 14272–14276 (2016).
- 365 11. Shimizu, S. *et al.* Giant thermoelectric power factor in ultrathin fese superconductor. *Nat.*  
366 *Commun.* **10**, 1–7 (2019).
- 367 12. Hicks, L. D. & Dresselhaus, M. S. Thermoelectric figure of merit of a one-dimensional  
368 conductor. *Phys. Rev. B* **47**, 16631–16634 (1993).
- 369 13. Mahan, G. D. & Sofo, J. O. The best thermoelectric. *Proc. Natl. Acad. Sci.* **93**, 7436–7439  
370 (1996).
- 371 14. Gao, W. *et al.* Macroscopically aligned carbon nanotubes for flexible and high-temperature  
372 electronics, optoelectronics, and thermoelectrics. *J. Phys. D* **53**, 063001 (2020).
- 373 15. Taylor, L. W. *et al.* Improved properties, increased production, and the path to broad  
374 adoption of carbon nanotube fibers. *Carbon* **171**, 689–694 (2021).
- 375 16. Behabtu, N. *et al.* Strong, light, multifunctional fibers of carbon nanotubes with ultrahigh  
376 conductivity. *Science* **339**, 182–186 (2013).
- 377 17. Adnan, M. *et al.* Bending behavior of cnt fibers and their scaling laws. *Soft Matter* **14**,  
378 8284–8292 (2018).
- 379 18. Nanot, S. *et al.* Single-walled carbon nanotubes. In Vajtai, R. (ed.) *Handbook of Nanoma-*  
380 *terials*, 105–146 (Springer, Berlin, 2013).
- 381 19. Nakai, Y. *et al.* Giant Seebeck coefficient in semiconducting single-wall carbon nanotube  
382 film. *Appl. Phys. Exp.* **7**, 025103 (2014).

- 383 20. Avery, A. D. *et al.* Tailored semiconducting carbon nanotube networks with enhanced  
384 thermoelectric properties. *Nat. Energy* **1**, 1–9 (2016).
- 385 21. Rowe, D. M. & Min, G.  $\alpha - \ln \sigma$  plot as a thermoelectric material performance indicator.  
386 *J. Mater. Sci.* **14**, 617–619 (1995).
- 387 22. Ichinose, Y. *et al.* Solving the Thermoelectric Trade-Off Problem with Metallic Carbon  
388 Nanotubes. *Nano Lett.* **19**, 7370–7376 (2019).
- 389 23. Hayashi, D. *et al.* Thermoelectric properties of single-wall carbon nanotube networks. *Jpn.*  
390 *J. Appl. Phys.* **58**, 075003 (2019).
- 391 24. An, C. J., Kang, Y. H., Song, H., Jeong, Y. & Cho, S. Y. High-performance flexible  
392 thermoelectric generator by control of electronic structure of directly spun carbon nanotube  
393 webs with various molecular dopants. *J. Mater. Chem. A* **5**, 15631–15639 (2017).
- 394 25. Cho, C. *et al.* Organic thermoelectric thin films with large p-type and n-type power factor.  
395 *J. Mater. Sci.* **56**, 4291–4304 (2021).
- 396 26. Mao, J., Chen, G. & Ren, Z. Thermoelectric cooling materials. *Nat. Mater.* 1–8 (2020).
- 397 27. Romero, H. E., Sumanasekera, G. U., Mahan, G. D. & Eklund, P. C. Thermoelectric power  
398 of single-walled carbon nanotube films. *Phys. Rev. B* **65**, 1–6 (2002).
- 399 28. Esfarjani, K., Zebarjadi, M. & Kawazoe, Y. Thermoelectric properties of a nanocontact  
400 made of two-capped single-wall carbon nanotubes calculated within the tight-binding ap-  
401 proximation. *Phys. Rev. B* **73**, 085406 (2006).

- 402 29. Yanagi, K. *et al.* Tuning of the thermoelectric properties of one-dimensional material  
403 networks by electric double layer techniques using ionic liquids. *Nano Lett.* **14**, 6437–  
404 6442 (2014).
- 405 30. Zhang, L. *et al.* Fiber-based thermoelectric generators: Materials, device structures, fabri-  
406 cation, characterization, and applications. *Adv. Energy Mater.* **8**, 1700524 (2018).
- 407 31. Wang, L. *et al.* Application challenges in fiber and textile electronics. *Adv. Mater.* **32**,  
408 1901971 (2020).
- 409 32. Loke, G., Yan, W., Khudiyev, T., Noel, G. & Fink, Y. Recent progress and perspectives of  
410 thermally drawn multimaterial fiber electronics. *Adv. Mater.* **32**, 1904911 (2020).
- 411 33. Lee, J., Llerena Zambrano, B., Woo, J., Yoon, K. & Lee, T. Recent advances in 1d stretch-  
412 able electrodes and devices for textile and wearable electronics: materials, fabrications,  
413 and applications. *Adv. Mater.* **32**, 1902532 (2020).
- 414 34. Zubair, A. *et al.* Carbon nanotube woven textile photodetector. *Phys. Rev. Materials* **2**,  
415 015201 (2018).
- 416 35. Lee, J. A. *et al.* Woven-yarn thermoelectric textiles. *Adv. Mater.* **28**, 5038–5044 (2016).
- 417 36. Sun, T. *et al.* Stretchable fabric generates electric power from woven thermoelectric fibers.  
418 *Nat. Commun.* **11**, 1–10 (2020).
- 419 37. Zhou, W. B. *et al.* Ultrahigh-power-factor carbon nanotubes and an ingenious strategy for  
420 thermoelectric performance evaluation. *Small* **12**, 3407–3414 (2016).
- 421 38. Choi, J. *et al.* Flexible and robust thermoelectric generators based on all-carbon nanotube  
422 yarn without metal electrodes. *ACS Nano* **11**, 7608–7614 (2017).

- 423 39. MacLeod, B. A. *et al.* Large n-and p-type thermoelectric power factors from doped semi-  
424 conducting single-walled carbon nanotube thin films. *Energy Environ. Sci.* **10**, 2168–2179  
425 (2017).
- 426 40. Cho, C. *et al.* Completely organic multilayer thin film with thermoelectric power factor  
427 rivaling inorganic tellurides. *Adv. Mater.* **27**, 2996–3001 (2015).
- 428 41. Cho, C. *et al.* Outstanding Low Temperature Thermoelectric Power Factor from Com-  
429 pletely Organic Thin Films Enabled by Multidimensional Conjugated Nanomaterials. *Adv.*  
430 *Energy Mater.* **6**, 1502168 (2016).
- 431 42. Watzman, S. J. *et al.* Magnon-drag thermopower and nernst coefficient in fe, co, and ni.  
432 *Phys. Rev. B* **94**, 144407 (2016).
- 433 43. Rowe, D., Kuznetsov, V., Kuznetsova, L. & Min, G. Electrical and thermal transport  
434 properties of intermediate-valence ybal3. *J. Phys. D: Appl. Phys.* **35**, 2183 (2002).
- 435 44. Boona, S. & Morelli, D. Enhanced thermoelectric properties of cepd3- xptx. *Appl. Phys.*  
436 *Lett.* **101**, 101909 (2012).
- 437 45. Yarbrough, D., Williams, R. & Graves, R. Transport properties of concentrated ag-pd and  
438 cu-ni alloys from 300–1000 k. In *Thermal Conductivity 16*, 319–324 (Springer, 1983).
- 439 46. Ishiwata, S. *et al.* Extremely high electron mobility in a phonon-glass semimetal. *Nat.*  
440 *Mater.* **12**, 512–517 (2013).
- 441 47. Pan, Y. *et al.* Mg<sub>3</sub>(bi, sb)<sub>2</sub> single crystals towards high thermoelectric performance.  
442 *Energy Environ. Sci.* (2020).

443 48. Tsentalovich, D. E. *et al.* Relationship of Extensional Viscosity and Liquid Crystalline  
444 Transition to Length Distribution in Carbon Nanotube Solutions. *Macromolecules* **49**, 681–  
445 689 (2016).

446 **Acknowledgements:** N.K. and J.K. acknowledge support by the Basic Energy Science (BES) pro-  
447 gram of the U.S. Department of Energy through Grant No. DE-FG02-06ER46308 (for prepa-  
448 ration of aligned carbon nanotube films), the U.S. National Science Foundation through Grant  
449 No. ECCS-1708315 (for optical measurements), and the Robert A. Welch Foundation through  
450 Grant No. C-1509 (for structural characterization measurements). K.Y. acknowledges support  
451 by JSPS KAKENHI through Grant Numbers JP17H06124, JP17H01069, and JP18H01816 and  
452 the JST CREST program through Grant Number JPMJCR17I5, Japan. We acknowledge the  
453 use of at Rice University. O.S.D., L.W.T., M.T., and M.P. acknowledge support by the U.S.  
454 Air Force research through Grant No. FA9550-15-1-0370, the Robert A. Welch Foundation  
455 through Grant C-1668, and the Department of Energy awards DE-EE0007865 (Office of En-  
456 ergy Efficiency and Renewable Energy – Advanced Manufacturing Office) and DE-AR0001015  
457 (Advanced Research Projects Agency – Energy). L.W.T. was supported by the Department of  
458 Defense through a National Defense Science and Engineering Graduate (NDSEG) Fellowship,  
459 32 CFR 168a. O.S.D. was partially supported by a Riki Kobayashi Fellowship from the Rice  
460 Chemical & Biomolecular Engineering Department. We thank the staff and facilities of the  
461 Shared Equipment Authority at Rice University, including the Electron Microscopy Center.

462 **Author contributions:** N.K. and J.K. conceived the project. N.K. and Y.I. performed measure-  
463 ments, analyzed experimental data, and prepared the manuscript under the supervision of Y.Y.,  
464 K.Y., and J.K. O.S.D. and L.W.T. prepared the fiber samples, and M.T. conducted doping, under  
465 the supervision of M.P. All authors discussed the results and commented on the manuscript.

466 **Competing interests:** The authors have no competing financial interest(s).

# Figures

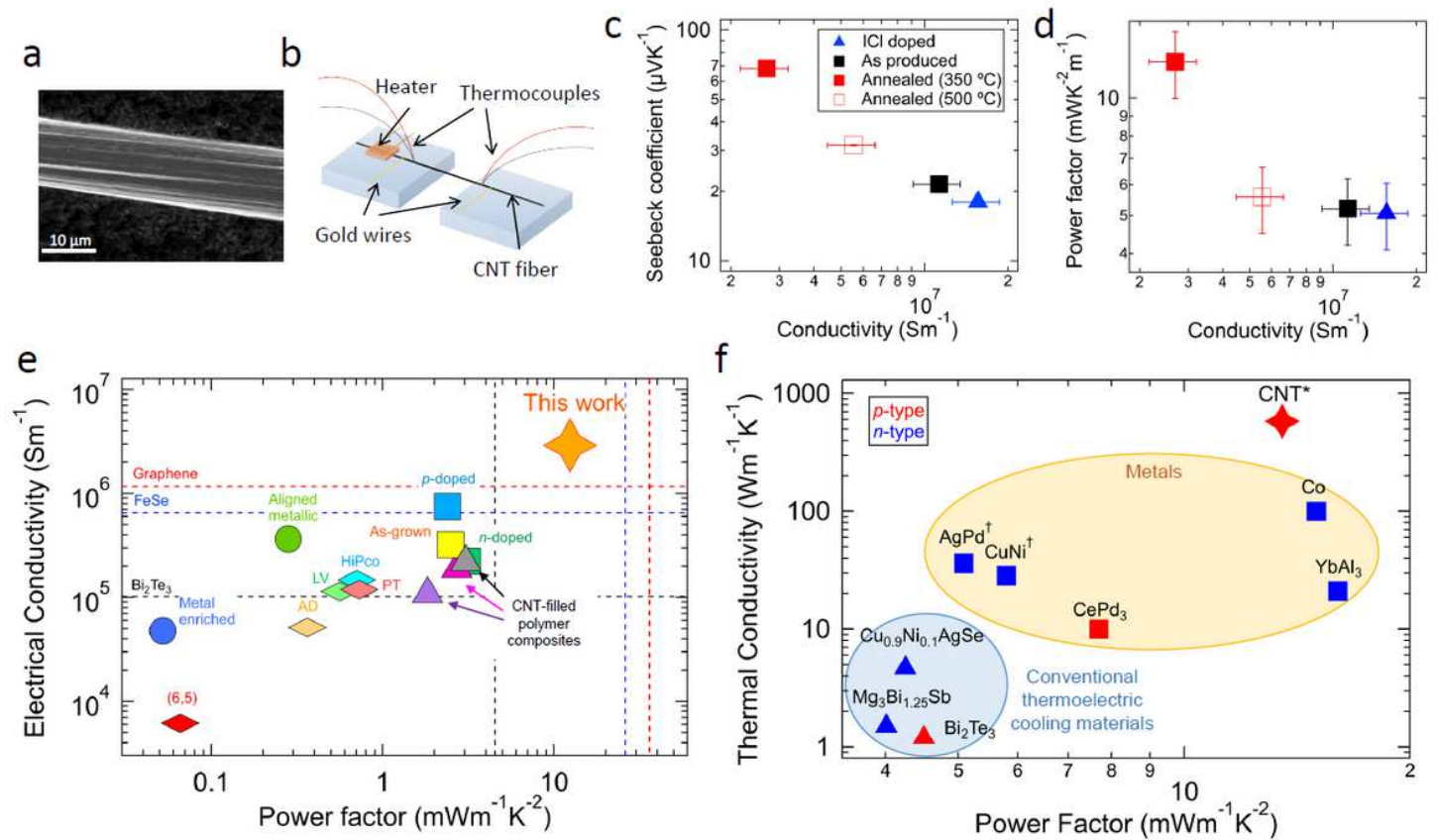


**Figure 1**

Thermoelectric properties of densely packed and highly aligned CNT fibers. a, SEM image of a CNT fiber. b, Schematic of the experimental setup used for measuring the electrical conductivity ( $\sigma$ ) and Seebeck coefficient ( $S$ ) of CNT fibers. c, Measured  $S$  and d, corresponding power factor ( $P F = S^2\sigma$ ) as a function of  $\sigma$  for four CNT fibers that underwent different chemical treatments: ICl doped (solid blue triangles), as-produced (solid black circles), annealed at 350 °C (open red squares), and annealed at 500 °C (solid red squares). The values are summarized in Supplementary Table S1. e, Comparison of reported  $P F$  values for various CNT samples with  $\sigma$ . The plot includes unsorted CNTs (as-grown (yellow square) 37, p-doped (blue square) 38 and n-doped (green square) 24), semiconductor-enriched SWCNTs (originally produced by arc-discharge (AD) (orange diamond) 39, by laser vaporization (LV) (green diamond) 39, by HiPco (blue diamond) 39, by plasma torch (PT) (pink diamond) 39, and (6,5) SWCNTs (red diamond) 22), metal-enriched SWCNTs (un-aligned films (blue circle) 22 and aligned films (green circle) 22), and CNT-filled polymer nanocomposites (PANI/graphene/PANI/DWCNT (purple triangle) 40, PANI/graphene-PEDOT:PSS/PANI/DWCNT-PEDOT:PSS (pink triangle) 41, and PANI/graphene/PANI/DWCNT (gray triangle) 25). Values are summarized in Supplementary Table S3.  $P F$  values of Bi<sub>2</sub>Te<sub>3</sub> alloys 9, graphene 10, and FeSe 11 serve as references. f, Comparison of reported  $P F$  values for representative materials with  $\kappa$  at 300 K with a  $\Delta T$  of 1 K. The plot includes metals (squares) (Co 42), YbAl<sub>3</sub> 43, CePd<sub>3</sub> 44, CuNi 45, and AgPd 45) and conventional thermoelectric cooling materials (triangles) (Bi<sub>2</sub>Te<sub>3</sub> 9, Cu<sub>0.9</sub>Ni<sub>0.1</sub>AgSe

46, and Mg<sub>3</sub>Bi<sub>1.25</sub>Sb<sub>47</sub>). p-type (n-type) materials are highlighted in red (blue). † The temperature was at 400 K because values at 300 K were not available. \* Thermal conductivity value was taken from Ref. 16. Values are summarized in Supplementary Table S4.

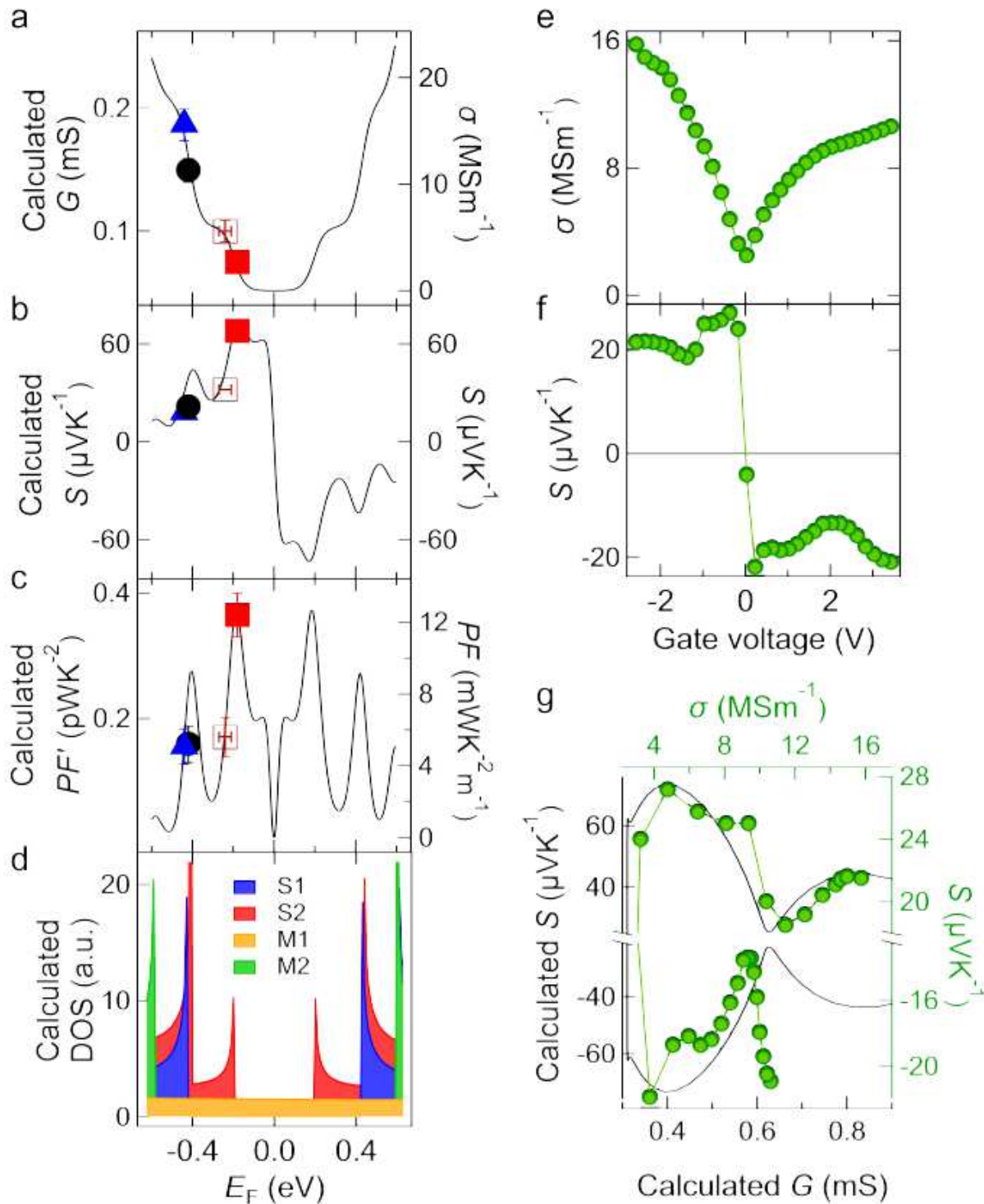


**Figure 2**

Explaining the EF dependent TE properties of CNT fibers through modeling. a, Calculated conductance  $G$ , b,  $S$ , and c,  $PF$  versus  $E_F$  (left) versus  $E_F$ . Experimental data from four chemically treated samples are

shown by different symbols on the right axis: ICI doped (solid blue triangle), as-produced (solid black circle), annealed at 350 °C (open red square), and annealed at 500 °C (solid red square). d, the DOS of four representative SWCNTs contained in our CNT fibers, S1 (blue), S2 (red), M1 (orange), and M2 (green). e and f, TE properties tuned by the electrolyte gating technique. e, Measured  $\sigma$  and f,  $S$  as a function of gate voltage. g, Comparison of calculated  $S$  (left) as a function of  $G$  (bottom) with experimental  $S$  (right) as a function of  $\sigma$  (top) with an offset in the x-axis such that the examined range by the experiments agrees. The calculated  $S$  is plotted with a black line, and the experimental data for gated samples are shown by a green line with solid circles.

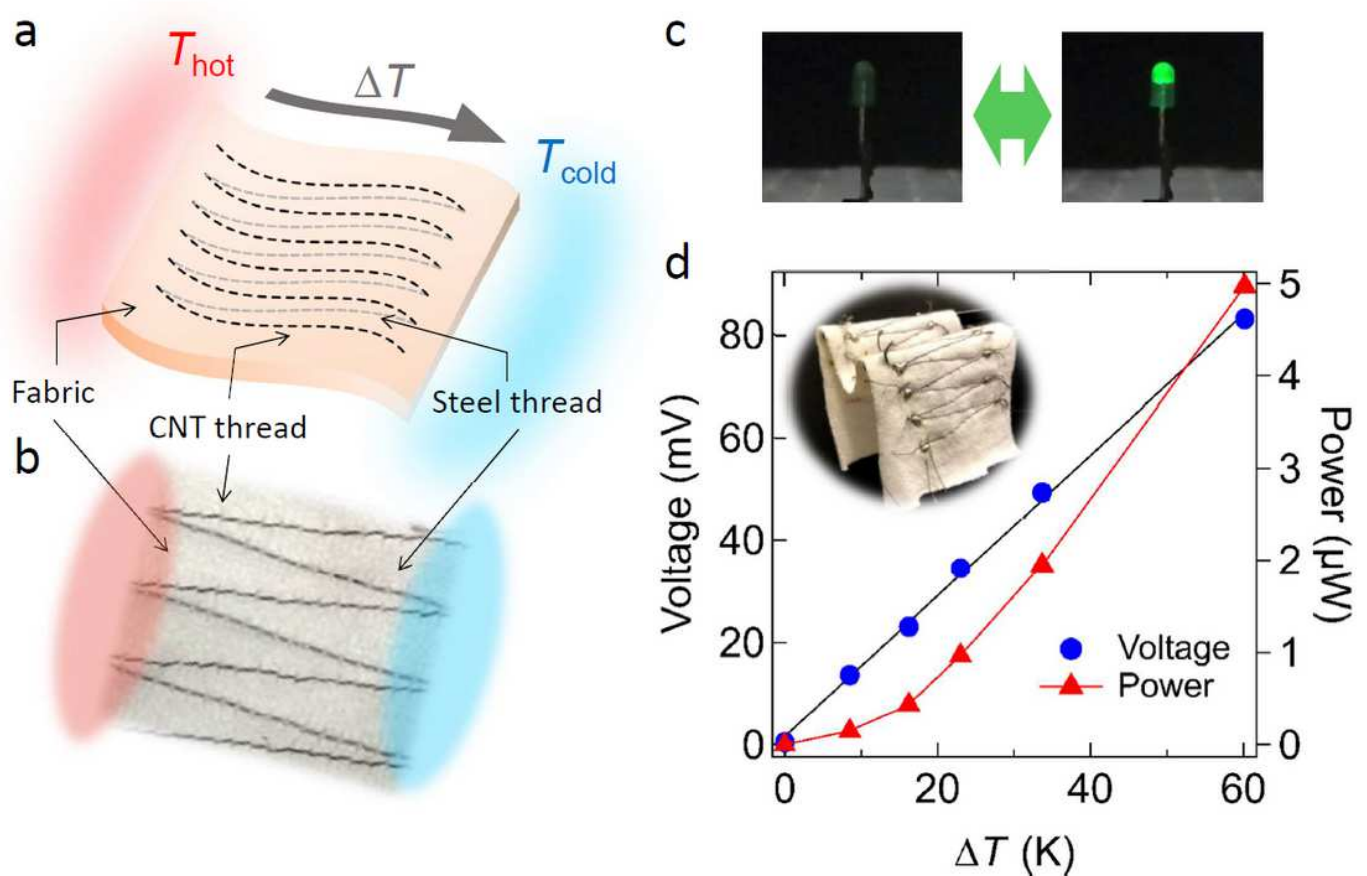


**Figure 3**

Textile TE generator based on CNT threads sewn into a fabric. a, Schematic and b, photograph of the device. CNT threads (p-type thermoelectric generator) and steel threads (for electrical connection) were sewn into a fabric using a sewing machine. The CNT threads were connected electrically in series and thermally in parallel. A temperature difference  $\Delta T$  was applied by heating one side ( $T_{hot}$ ) while keeping the other side ( $T_{cold}$ ) at room temperature. c, The entire device was connected to an LED through an amplification circuit and a capacitor. The LED turned on with a  $\Delta T$  of  $\approx 50$  K. d, Output voltage and power as a function of applied  $\Delta T$ . The inset shows a folded device, demonstrating its flexibility.

## Supplementary Files

This is a list of supplementary files associated with this preprint. Click to download.

- [finalvideo.mp4](#)
- [SI20210316.pdf](#)